AIAA JOURNAL
Vol. 39, No. 8, August 2001

Computational and Experimental Study of Linear Aerospike Engine Noise

Abdelkader Frendi*
University of Alabama in Huntsville, Huntsville, Alabama 35899
and
Tomas E. Nesman† and Ten-See Wang‡
NASA Marshall Space Flight Center, Huntsville, Alabama 35812

Experimental and computational results of X-33 linear aerospike engine noise tests are presented. Only noise sources external to the nozzle are considered (no combustion noise). The experimental setup is such that the engine, located 18.3 m above the ground, has its exhaust plume diverted from a vertical position to a nearly horizontal position located 3 m above the ground using a J deflector. Experimental measurements are made at several locations in the midfield. A semi-empirical model is derived that accounts for the nonaxisymmetry of the engine exit plane. The model uses mean flow quantities obtained from a computational fluid dynamics computation using a k–ε turbulence model. Midfield results obtained using the semi-empirical model are in reasonable agreement with the experimental measurements. The semi-empirical model was able to explain the source of a low-frequency peak observed in the spectra (near 10 Hz). In addition, the midfield directivity pattern and overall sound pressure levels given by the semi-empirical model are in good agreement with the measurements.

I. Introduction

In the past 50 years the problem of jet noise has been investigated extensively experimentally, analytically, and computationally. Interest in jet noise has been driven by the ever-increasing importance of the airplane for transportation and as a military machine. As we move into the 21st century, this interest will grow because of increasing regulations on community and passenger noise. In addition, future space transportation vehicles, such as the X-33, will have to be quieter at takeoff and landing to be used on regular airport runways. All of this requires fundamental understanding of the mechanisms responsible for jet noise.

The most important contribution to jet noise studies is due to Lighthill,[1,2] who used the basic fluid dynamic equations to derive the well-known Lighthill acoustic analogy. This equation gives the sound pressure at a far-field point radiated by a localized unsteady source or turbulent flow. Ribner[3] used the Lighthill acoustic analogy[1,2] to arrive at a relation between the mean-square pressure radiated by a jet plume into the far field as the integral over the plume volume of quadrupole correlations. Ribner[4,5] also showed the importance of convection and refraction on the far-field jet noise. Several other significant contributions to jet noise theory have been made by various researchers and are summarized in the review papers by Ffowcs Williams,[6,7] Goldstein,[8] and Tam.[9]

Mani et al.[10] used the Ribner[3] and the Ffowcs Williams[11] jet noise models in their extensive studies on high-velocity jet noise. Good agreement was obtained between the model and the experimental results for various nozzle geometries and flow regimes. More recently, Khavaran et al.[12] used a k–ε turbulence model to compute the jet mixing noise from a supersonic axisymmetric converging–diverging nozzle. They used the Mani et al.[10] approach to arrive at their results. Comparisons with experiments showed good agreement. Other computational studies using the k–ε turbulence model were carried out, for example, in Refs. 13 and 14, with varying degrees of success. Recently, Tam et al.[15] proposed a self-contained, semi-empirical jet noise theory for the prediction of fine-scale turbulence noise from high-speed jets. The theory uses jet flow turbulence information supplied by a k–ε turbulence model. In addition to the empirical constants found in a k–ε turbulence model, three empirical constants were added in the proposed jet noise theory. Noise predictions obtained from the new theory were in excellent agreement with measurements. The new theory uses linearized Euler equations to determine the far-field acoustic pressure, which is a departure from the widely used Lighthill acoustic analogy.[1,2]

In this paper, the model used by Mani et al.[10] is extended to a nonaxisymmetric jet. The mean flow results are obtained from a computational fluid dynamics (CFD) computation using a k–ε turbulence model. Experimental results from the X-33 engine tests conducted by the second author at NASA Stennis Space Center are used. The remainder of the paper is organized as follows: The details of the model are given in Sec. II, Sec. III gives the experimental setup, and Sec. IV describes the solution methodology. The results and discussions are summarized in Sec. V, and the concluding remarks are given in Sec. VI.

II. Mathematical Model

Just as Reynolds[16] revolutionized the study of fluid dynamics, Lighthill[1,2] made one of the most significant contributions to the study of aerodynamic noise. His famous equation, derived from the fundamental principals of fluid dynamics, is known as the Lighthill acoustic analogy and is widely used in the study of acoustics from any volumetric source. In the far field, this equation can be written as

$$p(\boldsymbol{R}, t) = \frac{R_i R_j}{4\pi C_\infty^2 R^3} \int_V \left[\frac{\partial^2 T_{ij}}{\partial t^2} \right] \mathrm{d}^3 \boldsymbol{y} \tag{1}$$

where T_{ij} is the Lighthill stress tensor given by

$$T_{ij} = \rho v_i v_j + \tau_{ij} + \left(\pi - C_\infty^2 \rho\right)\delta_{ij} \tag{2}$$

In Eq. (2), the dominant term is the unsteady momentum flux $\rho v_i v_j$. Also, τ_{ij} is the viscous compressive stress tensor, π the local pressure, ρ the density, C_∞ the ambient speed of sound, v_i the velocity, and δ_{ij} the Kronecker symbol (=0 if $i \neq j$ and =1 if $i = j$). The notation [ ] in Eq. (1) denotes evaluation at the retarded time, $\tau = t - \boldsymbol{R}/C_\infty$. On retaining the dominant term,[17] that is, $\rho v_i v_j$, the mean square pressure $\overline{p^2}$ radiated in the observer direction $(\boldsymbol{R}, \theta, \phi)$ in polar coordinates (see Fig. 1) can be written as

$$\overline{p^2}(\boldsymbol{R}, \theta, \phi) = \frac{R_i R_j R_k R_l}{16\pi^2 C_\infty^4 R^6} \int_V \int_V \overline{\frac{\partial^2(\rho v_i v_j)\partial^2(\rho v_k' v_l')}{\partial t'^2 \partial''^2}}\, \mathrm{d}^3 \boldsymbol{y}'\, \mathrm{d}^3 \boldsymbol{y}'' \tag{3}$$

Received 8 August 2000; revision received 15 January 2001; accepted for publication 30 January 2001.

*Associate Professor, Mechanical and Aerospace Engineering Department, TH N264. Senior Member AIAA.
†Aerospace Engineer, Space Transportation Directorate. Senior Member AIAA.
‡Team Leader, Applied Fluid Dynamics Analysis Group. Senior Member AIAA.

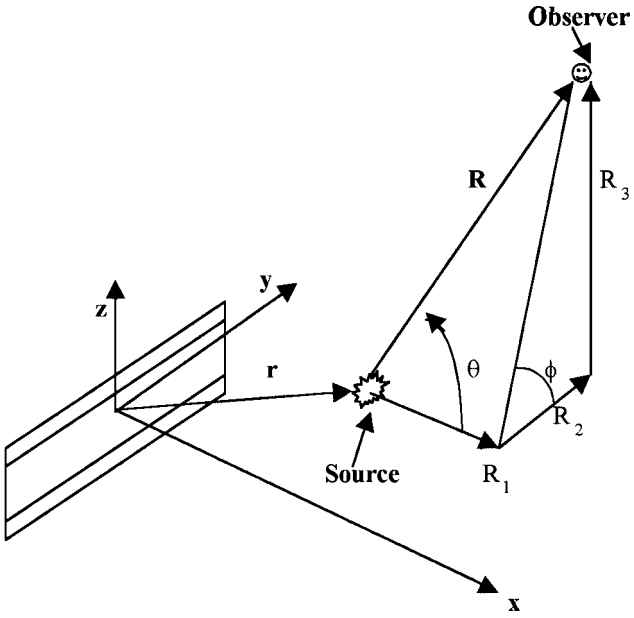

Fig. 1 Reference coordinate system.

The first term under the overbar is evaluated at (y', t'), whereas the second term is evaluated at (y'', t''). The emission times t' and t'' are retarded with respect to the reception time t. The quadrupole correlation shown with an overbar can be expressed as a function of the midpoint $\boldsymbol{y}$ and the separation in space and time:

$$\boldsymbol{y} = \tfrac{1}{2}(\boldsymbol{y}' + \boldsymbol{y}''), \qquad \boldsymbol{r} = \boldsymbol{y}' - \boldsymbol{y}'', \qquad \tau = t' - t'' \tag{4}$$

If the observer distance R is large compared to the flow dimensions, then

$$C_\infty \tau \cong \boldsymbol{r} \cdot \boldsymbol{R}/R \tag{5}$$

A convenient transformation of Eq. (3) is

$$\overline{p^2}(\boldsymbol{R}, \theta, \phi) = \frac{R_i R_j R_k R_l}{16\pi^2 C_\infty^4 R^6} \int_V \frac{\partial^4}{\partial \tau^4} \overline{(\rho v_i v_j)(\rho' v_k' v_l')}\, \mathrm{d}^3\boldsymbol{r} \tag{6}$$

Ribner[3] has shown that for an axisymmetric source field and for a locally isotropic turbulent field, only a few of the 81 possible combination of indices i, j, k, and l have a significant contribution. When the turbulence is assumed quasi incompressible, Eq. (6) becomes

$$\overline{p^2}(\boldsymbol{R}, \theta, \phi) = \frac{\rho^2 R_i R_j R_k R_l}{16\pi^2 C_\infty^4 R^6} \int_V \frac{\partial^4}{\partial \tau^4} \overline{v_i v_j v_k' v_l'}\, \mathrm{d}^3\boldsymbol{r} \tag{7}$$

where $S_{ijkl} = \overline{v_i v_j v_k' v_l'}$ is the fourth-order velocity correlation tensor. Ribner[3] expressed S_{ijkl} in terms of linear combinations of second-order correlations as follows:

$$S_{ijkl} = S_{ik} S_{jl} + S_{il} S_{jk} + S_{ij} S_{kl} \tag{8}$$

where $S_{ij} = \overline{v_i v_j'}$. The various source terms are then evaluated using the isotropic turbulence model of Batchelor[18] and by assuming that the second-order correlations are separable functions of $\boldsymbol{r}$ and τ:

$$S_{ij}(\boldsymbol{r}, \tau) = \Lambda_{ij}(\boldsymbol{r}) g(\tau) \tag{9}$$

with

$$\Lambda_{ij}(r) = k\left[(f + \tfrac{1}{2} r f')\delta_{ij} - \tfrac{1}{2} f' r_i r_j / r\right] \tag{10}$$

where k is the local turbulence kinetic energy and f some universal function of r given by

$$f(r) = \exp(-\pi^2 r^2 / L^2) \qquad \text{with} \qquad r^2 = x^2 + y^2 + z^2 \tag{11}$$

In the preceding definition of f, L is a longitudinal macroscale of the turbulence. In Eq. (9), $g(\tau)$ is the time-delay factor assumed by Ribner[3] to be of the form

$$g(\tau) = \exp\left[-(\tau/\tau_0)^2\right] \tag{12}$$

where τ_0 is the characteristic time delay that determines the minimum significant correlation in a moving reference frame and is defined to be

$$\tau_0 = \left(c_t \frac{\partial U}{\partial n}\right)^{-1} \tag{13}$$

with c_t an empirical constant and $\partial U/\partial n$ given by

$$\frac{\partial U}{\partial n} = \sqrt{\left(\frac{\partial U}{\partial y}\right)^2 + \left(\frac{\partial U}{\partial z}\right)^2} \tag{14}$$

The length scale L in Eq. (11) is defined as

$$L = c_l k^{\frac{1}{2}} \tau_0 \tag{15}$$

where c_l is another empirical constant. Using Eqs. (8–15) in Eq. (7) and taking the Fourier transform of the resulting equation with respect to τ, we arrive at the spectrum

$$I(\Omega) = c_l^3 \rho^2 k^{\frac{7}{2}} (\Omega\tau_0)^4 e^{-\frac{1}{8}(\Omega\tau_0)^2} \tag{16}$$

where Ω is the source frequency, which is related to the observed frequency by[10,12]

$$\Omega = 2\pi f \sqrt{(1 - M_c \cos\theta)^2 + \left(c_d k^{\frac{1}{2}} / C_\infty\right)^2} \tag{17}$$

In Eq. (17), M_c is the convection Mach number given by

$$M_c = \tfrac{1}{2} M + c_c M_j \tag{18}$$

where M is the local Mach number, M_j is the nozzle exit Mach number, and c_c and c_d are empirical constants. Lighthill's acoustic analogy approach,[1,2] which is based on the classical wave equation, does not include the effects of the surrounding mean flow. Several studies were carried out to quantify the mean flow effects on sound radiation.[19,20] It is found that the mean flow results in not only the refraction of the radiated sound, but also in convection amplification due to fluid motion. The Mani et al.[6] formulation is used to link the turbulent properties of a jet plume to the radiated acoustic field as follows:

$$\overline{p^2}(R, \theta, \Omega) = \int_V \Psi(a_{xx} + 4a_{xy} + 2a_{yy} + 2a_{yz})\, \mathrm{d}^3 r \tag{19}$$

with Ψ given by

$$\Psi = \frac{I(\Omega)}{16\pi^2 R^2 C_\infty^4} \left(\frac{\rho_\infty}{\rho}\right)^2 \left(\frac{C_\infty}{C}\right)^2 (1 - M\cos\theta)^{-2} (1 - M_c \cos\theta)^{-1} \tag{20}$$

The directivity factors a_{xx}, a_{xy}, a_{yy}, and a_{yz} have different forms depending on the location of the source and the velocity and temperature profiles in the vicinity of the source. These factors depend explicitly on a shielding function g^2 that has the form

$$g^2(r) = \frac{(1 - M\cos\theta)^2 (C_\infty/C)^2 - \cos^2\theta}{(1 - M_c \cos\theta)^2} \tag{21}$$

When the location and the shape of the profiles, that is, velocity and temperature, are depended on, the function g^2 may have both positive and negative regions in space. When a negative region exists,

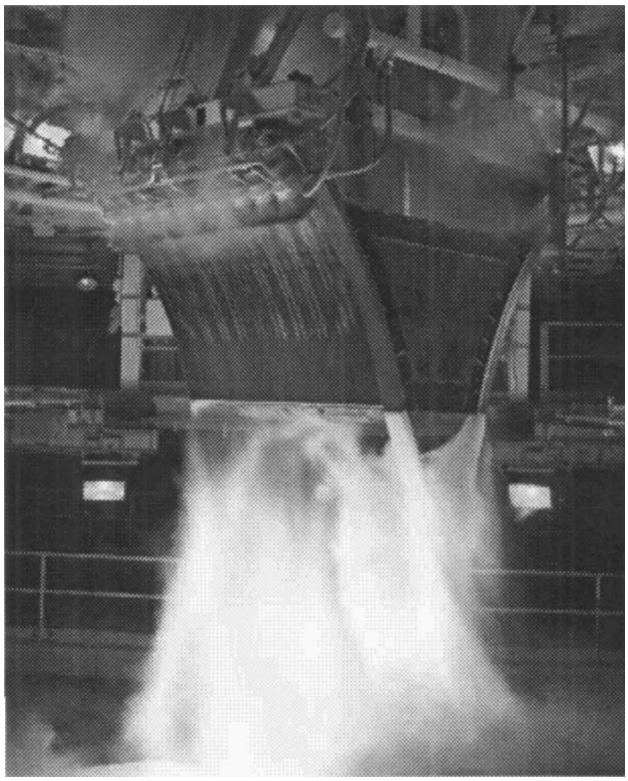

Fig. 2 Experimental setup and hotfire engine test.

fluid shielding of the source is possible. The directivity factors are given by

$$a_{xx} = \frac{\cos^4\theta}{(1 - M_c\cos\theta)^4}\beta_{xx} \tag{22a}$$

$$a_{xy} = \frac{g_0^2\cos^2\theta}{2(1 - M_c\cos\theta)^2}\beta_{xy} \tag{22b}$$

$$a_{yy} = \frac{3}{8}g_0^4\beta_{yy} \tag{22c}$$

$$a_{yz} = \frac{1}{8}g_0^4\beta_{yz} \tag{22d}$$

where g_0^2 is the value of $g^2(r)$ at the source radius $r = r_0$. The shielding coefficients β_{xx}, β_{xy}, β_{yy}, and β_{yz} depend on the location of the source and are set equal to one in the present study. A study on the effects of the shielding coefficients is currently under way.

III. Experimental Setup

The linear aerospike engine, XRS-2200, single engine tests were conducted at the Stennis Space Center in late 1999 and early 2000. The acoustic environment was measured during a series of 10 hotfire tests (Fig. 2). The engine was suspended above a J deflector, where the vertical distance (along the centerline of the engine) from the engine exit ramp plane to the deflector was 15.244 m. The nozzle ramp was 2.82×2.24 m at one end and 1.07×2.24 m at the other end, with a length of 1.27 m and an area ratio of 58. The jet Mach number was 3.042. Pressure transducers and microphones were arranged around the engine and test stand to determine the acoustic noise generated during testing. Microphones were also arranged at ground level at various distances and angles from the test stand, as shown in Fig. 3. Most of the microphones on the test stand were of the PCB Model 106B50, which has a relatively flat response for frequencies greater than 20 kHz. In addition, Kulite Model XCS-190-5D transducers were also used on the stand. The test stand microphones were recorded using a Teac XR-5000 video home system (VHS) tape recorder. The analog signal was recorded 5-V full scale at 76 cm/s tape speed in the FM high-bandwidth (HB) mode. The vented field microphones were 1.27 cm in diameter (B&K Models 4190 and 4191) except at locations near the test stand, where microphones of 0.632 cm in diameter (B&K Model 4138) were used. The microphone signal was preamplified (B&K Model 2669) and passed through shielded cabling to amplifiers (Nexus Model 2690), then through coaxial cables to a test stand recorder. The analog signal was recorded 5-V full scale at 76-cm/s tape speed in the FM mode using a Teac XR-510 VHS tape recorder. For the test stand microphones, a 24-mV signal was input at each transducer location and verified at the recorder input. The end-to-end step calibration signal was recorded on the Teac XR-5000 VHS recorder at a tape speed of 38 cm/s and an input voltage range of 5-V full scale. The signal conditioning consists of a PCB amplifier for the PCB microphones and a Pacific amplifier for the Kulite pressure transducers. For the B&K microphones, a calibrator (B&K Model 4231) was attached to each microphone, and the end-to-end signal from the 94 dB and 1000-Hz tone was recorded.

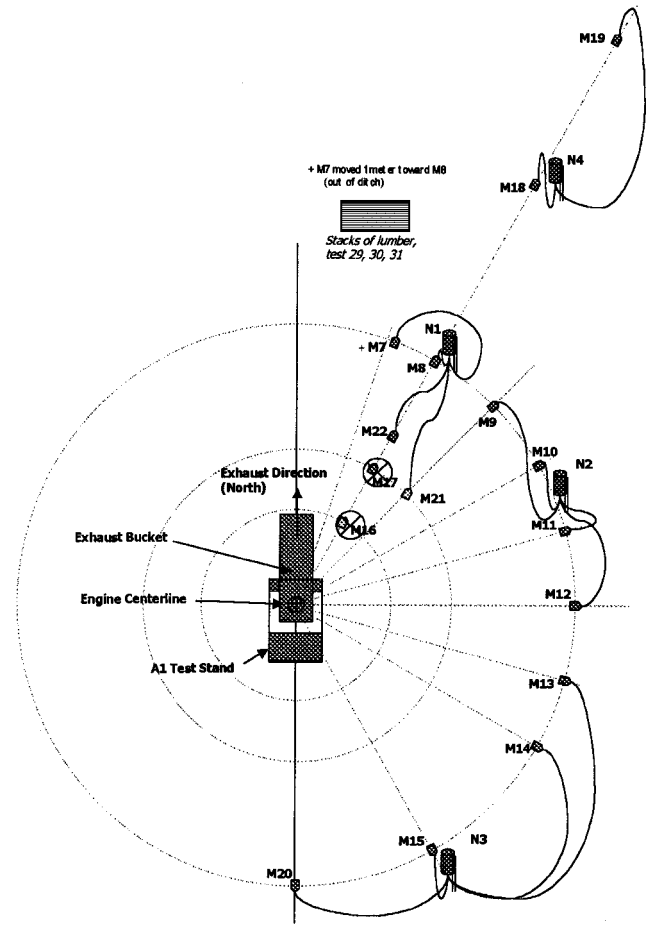

Fig. 3 Microphone locations in the midfield at 90 m from the test stand.

The frequency response of the microphones was 5 Hz–20 kHz and pressure transducers dc−10 kHz. The microphone full-scale record range was varied from 170 to 150 dB depending on location, and the pressure transducer range was ±5 psi differential. The background noise was measured and removed from the test data. Acoustic data at 34 different locations were successfully measured, recorded, and analyzed. These data provide a database for linear aerospike acoustic environment predictions. Spectral shapes, overall sound-pressure-level distributions, and decay rate were measured for the midfield.

IV. Method of Solution

A. Mean Flow Computation

The Reynolds-averaged Navier–Stokes equations are integrated over a domain 2.5 times the length of the X-33 vehicle of 25 m. The main CFD code used is known as FDNS.[21] The code uses a second-order finite difference scheme to discretize the diffusion fluxes and source terms of the governing equations. The convective terms are discretized using a second-order total-variation-diminishing difference scheme. The volume grid is composed of 2.2×10^6 grid points and is shown in Fig. 4. Details about the grid refinement techniques

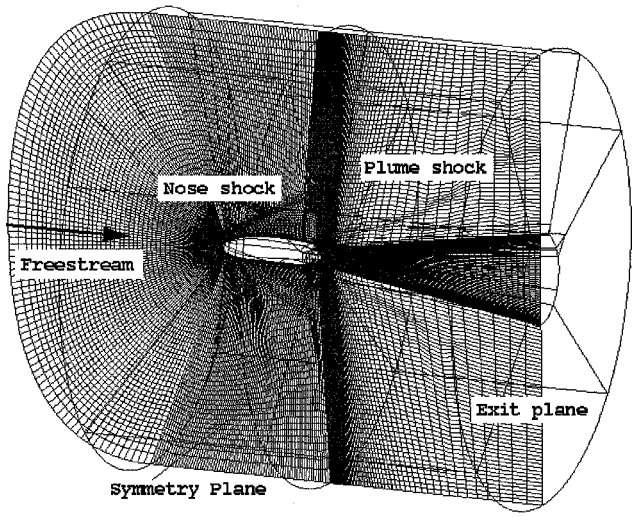

Fig. 4 Computational grid.

used and the treatment of the various boundary conditions and source terms can be found in Ref. 22. An extended k–ε turbulence model[23] is used to describe the turbulence.

B. Engine Noise Computation

By the use of the CFD results for the engine plume, integration of Eq. (19) over the entire plume volume is carried out. Because the geometry of the engine is not axisymmetric (which leads to a nonaxisymmetric flowfield), several computational techniques were introduced to take this into account. One of the key elements of the present model is the definition of the characteristic time delay τ_0, given by Eqs. (13) and (14). In most axisymmetric models, $\tau_0 \approx (\partial U/\partial r)^{-1} \approx k/\varepsilon$, with ε being the dissipation rate of the turbulent kinetic energy and r the radial coordinate. Equation (14) is necessary to take into account both the spanwise and vertical variations. In Eq. (18), the jet Mach number M_j is needed to compute the convection Mach number M_c. This is achieved by averaging the local Mach number M over the engine exit plane. Because the model used is derived from an existing axisymmetric model, averaging of all flow quantities in both the spanwise and vertical directions was used extensively. The total mean-square pressure at a given observer location is made up of the sum of the spanwise averaged result and the vertical averaged result as follows:

$$\overline{p_{\text{tot}}^2} = \tfrac{1}{2}\left[\overline{p_{\text{vert}}^2} + \overline{p_{\text{span}}^2}\right] \tag{23}$$

Given the direction in which averaging takes place, integration is then carried out over the remaining direction of the cross section. After this integration is performed over all of the cross sections, the streamwise integration of the results is then carried out to obtain the contribution of the total volume at a given observer frequency and location. This process is repeated for all observer frequencies and locations, R, θ, and ϕ. The trapezoidal rule of integration is used for all of the spatial integrals.

In the experimental setup, the engine plume is composed of two sections: one in which the plume is directed toward the ground for a distance of about 15.25 m from the engine exit plane and another where the plume is deflected. The deflection, referred to as a J deflection, sends the plume at an angle with the ground. The CFD computation was performed for a straight plume and was divided into 64 streamwise cross sections, each cross section is made up of 57 and 137 vertical and spanwise direction grid points, respectively. To account for the experimental plume deflection, the straight CFD plume is divided into two blocks: each block is assigned a different observer point for the same experimental measurement location. This is achieved by using two reference frames; one is centered at the beginning of the undeflected plume (engine exit plane) and the other at the beginning of the deflected plume. Both blocks are composed of 32 streamwise cross sections. This numerical treatment does not take into account any additional noise sources created by the deflection itself. A more accurate steady-state CFD computation that includes a J deflection is needed. Such a calculation is expensive and, therefore, not possible at the present time.

V. Results and Discussion

A. Mean Flow Results

The freestream parameters used in the computation are density $\rho_\infty = 1.2$ kg/m^3, temperature $T_\infty = 300$ K, and Mach number $M_\infty = 0$. The ratio of specific heats γ is set equal to 1.4. Figure 5 shows the temperature distribution in the plume region. The lateral and vertical extent and the nonaxisymmetry of the plume are clearly shown. In addition, Fig. 5 includes the interaction between the engine plume and the thrusters' plumes. The thrusters are located upstream of the engine exit plane. Figure 5 focuses only on the region near the engine exit plane, but the computation is carried out far downstream. The plume density contours at three downstream distances from the engine exit plane are shown in Fig. 6. Figure 6 shows that, as the distance from the engine increases, the plume becomes more axisymmetric. Figure 7 shows the lateral average of the turbulent kinetic energy profiles as a function of the vertical distance at three different downstream locations. Figure 7 also shows the asymmetry of the profiles caused by differences in geometry between the upper and lower surfaces. Figure 8 shows the variation of the vertical average of the turbulent kinetic energy with the lateral distance at the same three downstream locations. As expected, the profiles are symmetrical.

The vertical and lateral averages of the mean velocity profiles as a function of the lateral and vertical directions are shown in Figs. 9 and

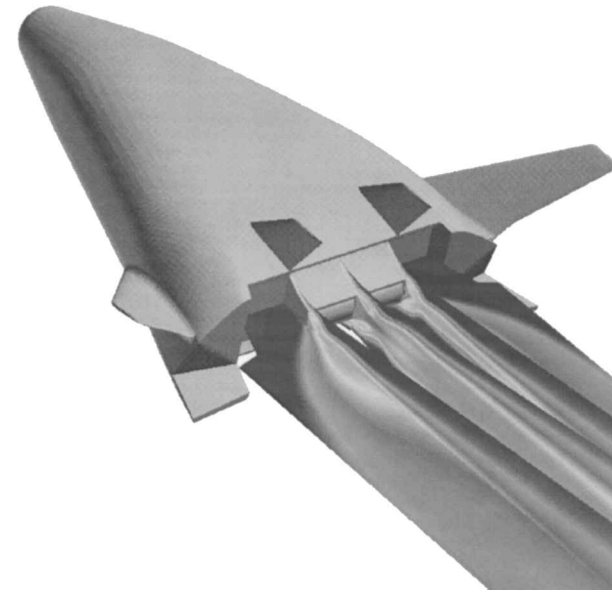

Fig. 5 Calculated temperature distribution in the plume region.

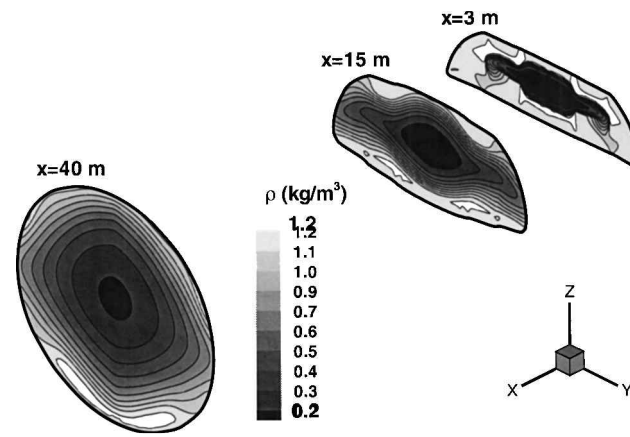

Fig. 6 Density contours at three downstream locations in the plume.

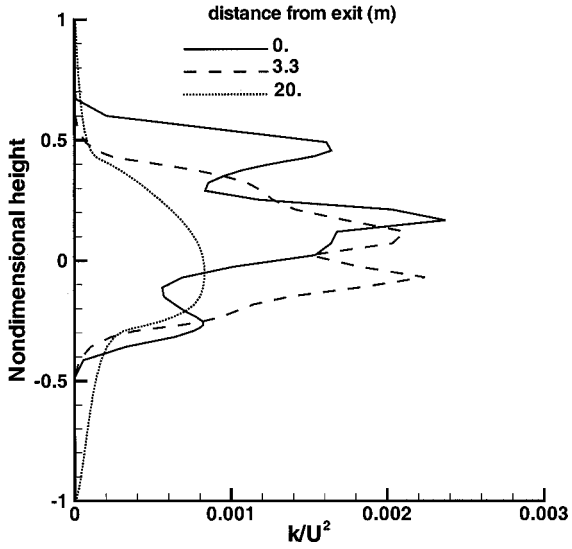

Fig. 7 Nondimensional vertical turbulent kinetic energy profiles at three downstream locations.

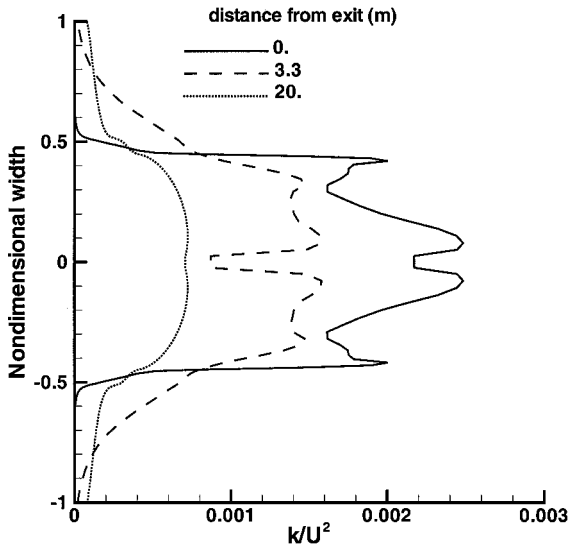

Fig. 8 Nondimensionallateral turbulent kinetic energy profiles at three downstream locations.

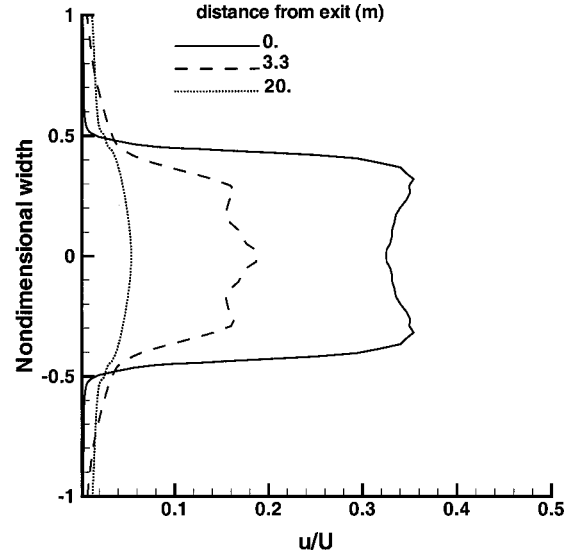

Fig. 9 Nondimensional lateral mean velocity profiles at three downstream locations.

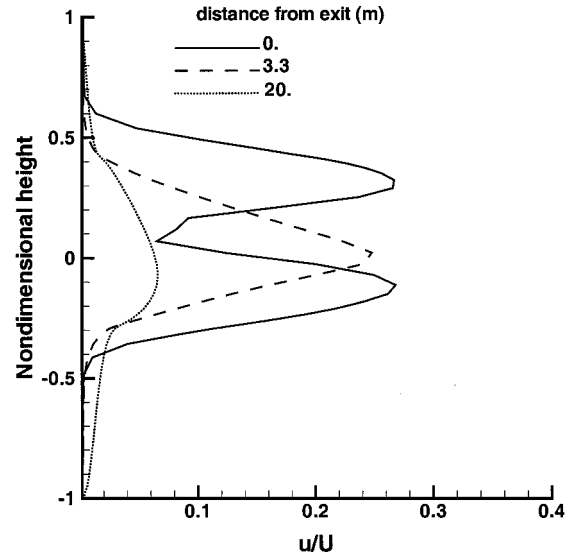

Fig. 10 Nondimensional vertical mean velocity profiles at three downstream locations.

10, respectively. Similar to the turbulent kinetic energy, the plume mean velocity profile is symmetrical in the lateral direction (Fig. 9) and asymmetrical in the vertical direction (Fig. 10). Both the velocity and turbulent kinetic energy profiles are nondimensionalized with the maximum local plume velocity of $U = 3500$ m/s. The lateral and vertical directions are nondimensionalized with the width and height of the engine, respectively.

B. Engine Noise Results

The first task to be performed is to select the four empirical constants of the model, c_c, c_d, c_l, and c_t. This is achieved by using a measured spectrum in one-third-octave frequency at a fixed observer location. Several measurements are made on the ground at a radius of 90 m from the test stand and at various angular locations with respect to the deflected plume (Fig. 3). Because of the experimental setup, the 90-deg location is chosen for calibration of the empirical constants. Figure 11 shows a comparison between the measured and calculated spectra. The calculated spectrum is in reasonable agreement with that of the measurement. The agreement is particularly good at low frequencies. In addition, just as in the experiment, the calculated spectrum shows the presence of two peaks. The location and level of the calculated peaks are in good agreement with those obtained experimentally. This agreement is obtained after few trial and error runs with different empirical constants. The final set of

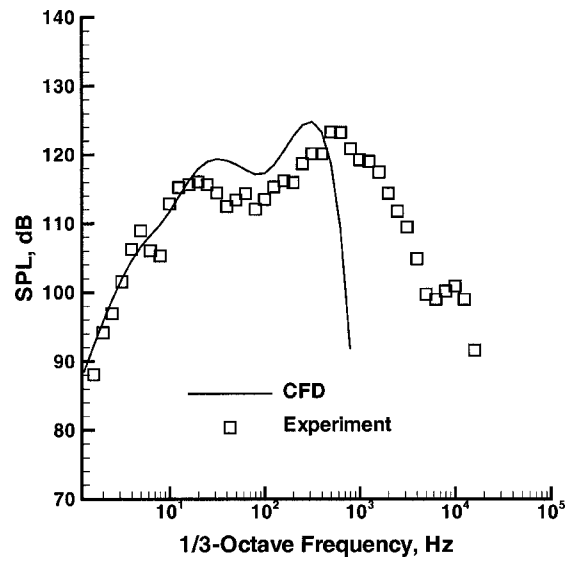

Fig. 11 Comparison of the calculated and measured spectrum at a midfield location 90 m from the test stand and at an angle of 90 deg with the deflected plume axis.

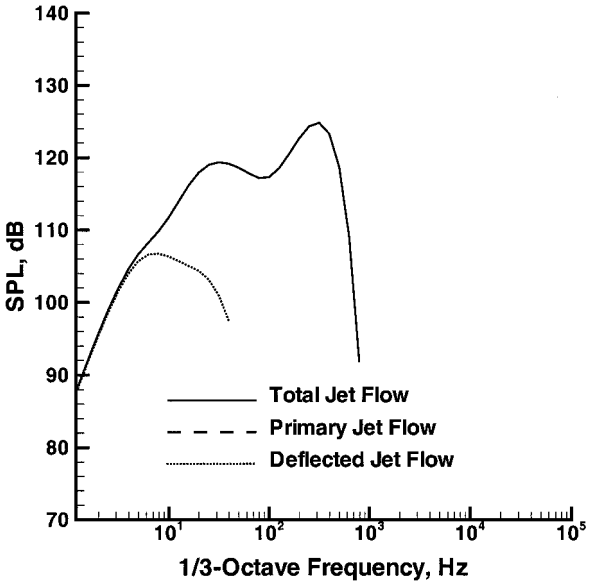

Fig. 12 Contributions of the deflected and undeflected plumes to the spectrum of Fig. 10.

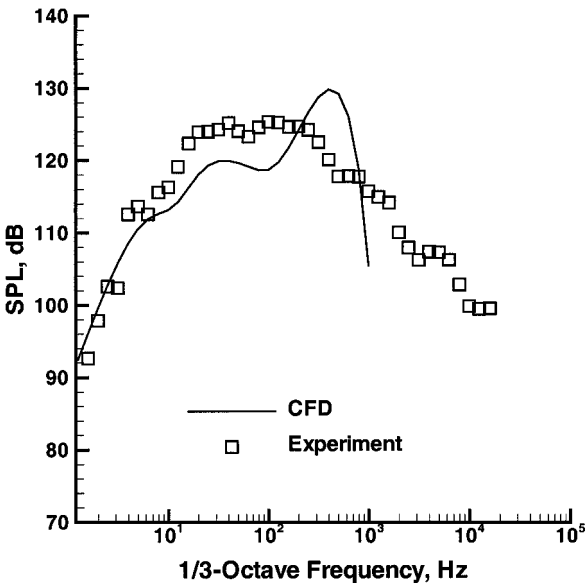

Fig. 13 Comparison of the calculated and measured spectrum at a midfield location 90 m from the test stand and at an angle of 22 deg with the deflected plume axis.

empirical constants selected is $c_c = 0.27$, $c_d = 0.55$, $c_t = 0.08$, and $c_l = 1.13$. In addition to the spectrum, the overall sound pressure level (OASPL) at the 90-deg location is used in choosing the constants. The poor agreement at high frequencies is partially attributed to an inadequate grid resolution. The CFD grid was initially constructed for base-heating purposes; that is, the grid was clustered around the engine and the base.[22]

To understand the spectrum of Fig. 11, the calculated results are divided into a contribution from the primary undeflected plume and that of the deflected plume. Figure 12 shows that the contribution from the deflected plume at this location is negligible. Figure 13 shows a comparison between a calculated and measured spectrum at a 22-deg angle with respect to the flow direction of the deflected plume. Once again the low frequency and the shape of the spectrum are in reasonably good agreement with the experimental measurements. However, the calculated high-frequency peak is shifted. The same empirical constants are used at this location. A better agreement could be achieved by changing the empirical constants. Further examination of the calculated spectrum shows the contribution of the different parts of the plume (Fig. 14). The contribution of the

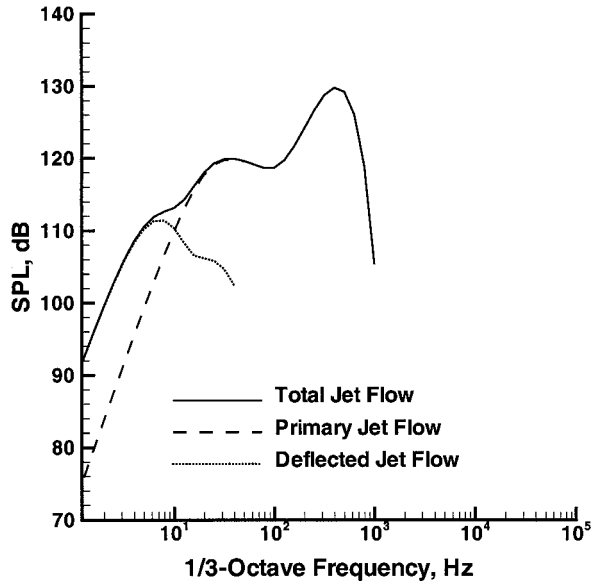

Fig. 14 Contributions of the deflected and undeflected plumes to the spectrum of Fig. 12.

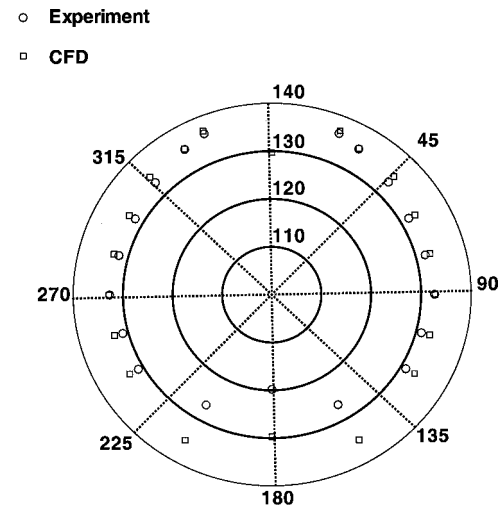

Fig. 15 Comparison of the calculated and measured directivity pattern at the midfield location of 90 m from the test stand.

deflected plume is to increase the level of the low frequencies (below 20 Hz). The calculated and measured directivity pattern at the midfield location is shown in Fig. 15. The OASPL is given at the various angular locations. Good agreement is obtained at most locations except the ones between 135 and 225 deg. In the experiment, these locations are sheltered by the stand and, therefore, are subjected to less noise. This is not the case in the calculation. Both the experimental data and the calculated results show a maximum OASPL level of 136.3 dB located at angles of 22 and 338 deg. Figure 16 shows the contribution of the undeflected (primary) and deflected plumes to the overall directivity pattern. Figure 16 also shows that the undeflected plume dominates the noise radiation at most angular locations except at 0 and 180 deg, where the deflected plume has a significant contribution. The calculated spectrum at an angle of 180 deg is shown in Fig. 17. The contribution of the deflected plume is given by a large peak near 10 Hz. The level of the high-frequency peak contributed by the primary plume is lower. The spectrum of the primary plume shows another peak around 40 Hz. Similar results are obtained at 0 deg.

Because measurements were made on the stand near the engine, a comparison is made at one location between the primary and deflected plumes at a downstream location from the engine exit plane of 1 m and a radius of 8.2 m. Figure 18 shows the calculated and measured spectra. The calculated spectrum is obtained by only

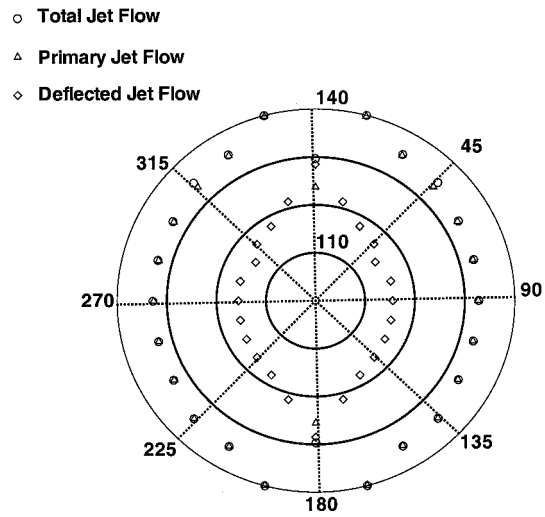

Fig. 16 Contribution of the deflected and undeflected plumes to the directivity pattern of Fig. 14.

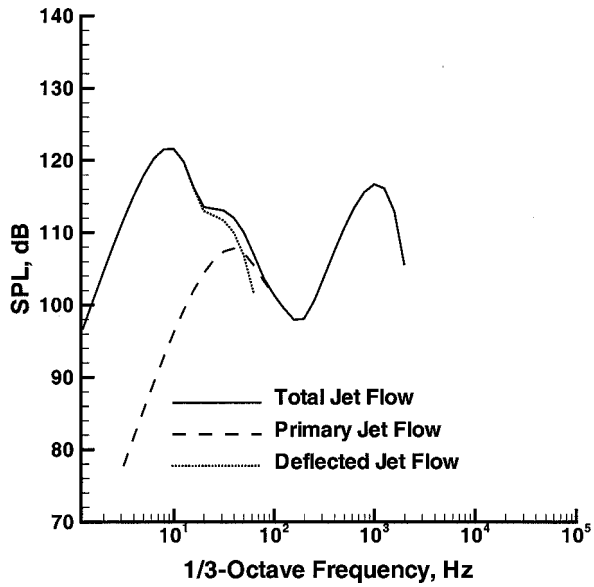

Fig. 17 One-third-octave frequency spectrum at the midfield location of 90 m and at an angle of 180 deg with deflected plume axis.

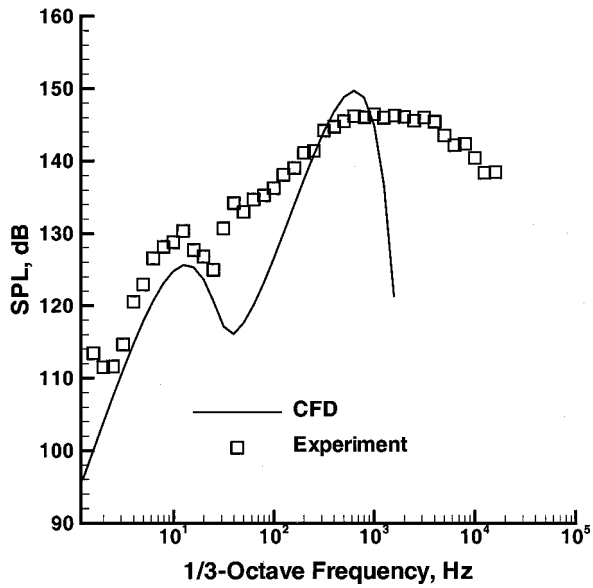

Fig. 18 Measured and calculated spectrum at a near-field location between the deflected and undeflected plumes.

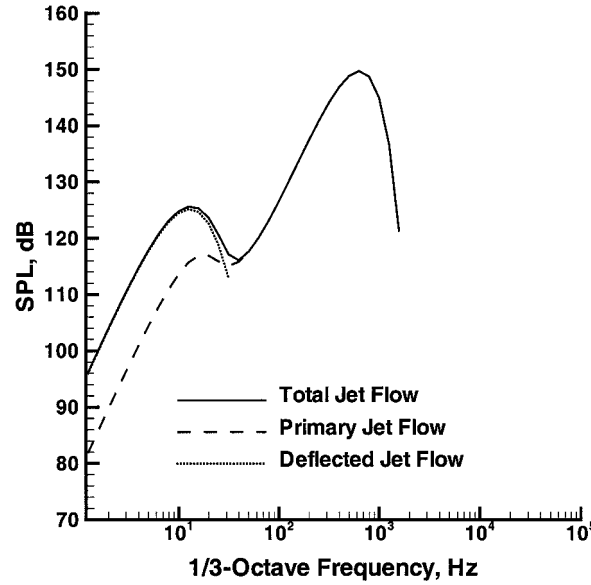

Fig. 19 Contributions of the deflected and undeflected plumes to the spectrum of Fig. 17.

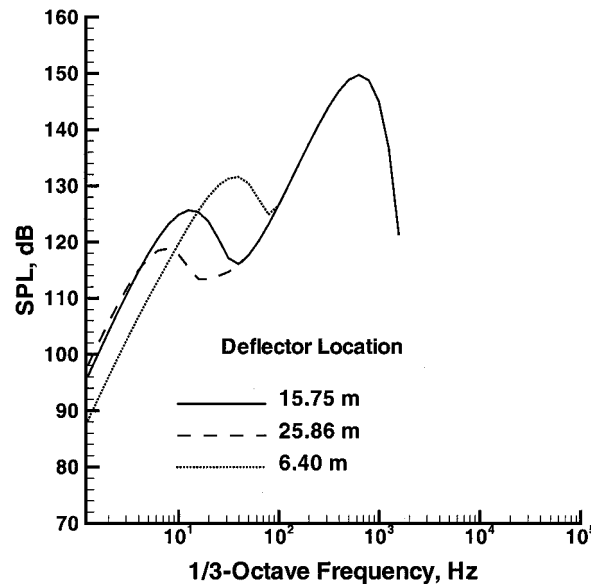

Fig. 20 Effect of the deflection location on the near-field spectrum.

adjusting one empirical constant, $c_c = 0.2$ (the model presented in this paper is a far-field model and, therefore, is not expected to perform well at locations closer to the engine plume). Both the calculated and measured spectra show two peaks, one near 10 Hz and the other near 1000 Hz. On further inspection of the calculated spectrum, it is shown that the deflected plume is responsible for the low-frequency peak, whereas the primary plume generates the high-frequency peak as shown in Fig. 19. Figure 20 shows the effect of the deflection location on the overall spectrum at the same nearfield location. The results show that by varying the deflection location between 6 and 26 m the low-frequency peak moves from 50 to 5 Hz and its level decreases from 132 to 118 dB, respectively.

VI. Conclusions

A semi-empirical acoustic radiation model is derived from the Lighthill acoustic analogy[1,2] to study the noise radiated by a linear aerospike engine. Because the engine is non-axisymmetric, a technique is introduced to take this into account while using the model derived by Ribner.[3] The model is calibrated using experimental data at a midfield location. The results show that the model is able to predict midfield spectra and directivity patterns that are in reasonable agreement with those measured. The model is subsequently used to

explain the various components of the spectra. It is found that the midfield directivity pattern at the given location is dictated by the undeflected plume. The deflected plume's contributionis to increase the level of the low frequencies (less than 20 Hz). A similar result is obtained at locations closer to the engine. The model showed that changing the deflection location resulted in changing the low-frequency peak and its level.

Acknowledgment

The first author would like to acknowledge the support of NASA Marshall Space Flight Center through a summer faculty fellowship grant.

References

[1]Lighthill, M. J., "On Sound Generated Aerodynamically: I. General Theory," *Proceedings of the Royal Society of London, Series A: Mathematical and Physical Sciences*, Vol. 211, March 1952, pp. 564–587.

[2]Lighthill, M. J., "On Sound Generated Aerodynamically: I. Turbulence as a Source of Sound," *Proceedings of the Royal Society of London, Series A: Mathematical and Physical Sciences*, Vol. 222, Feb. 1954, pp. 1–32.

[3]Ribner, H. S., "Quadrupole Correlations Governing the Pattern of Jet Noise," *Journal of Fluid Mechanics*, Vol. 38, No. 1, 1969, pp. 1–24.

[4]Ribner, H. S., "On the Strength Distribution of Noise Sources Along a Jet," *Journal of the Acoustical Society of America*, Vol. 31, No. 1, 1958, pp. 245, 246.

[5]Ribner, H. S., "On Spectra and Directivity of Jet Noise," *Journal of the Acoustical Society of America*, Vol. 35, No. 4, 1963, pp. 614–616.

[6]Ffowcs Williams, J. E., "Hydrodynamics Noise," *Annual Review of Fluid Mechanics*, Vol. 1, 1969, pp. 197–222.

[7]Ffowcs Williams, J. E., "Aeroacoustics," *Annual Review of Fluid Mechanics*, Vol. 9, 1977, pp. 447–468.

[8]Goldstein, M. E., "Aeroacoustics of Turbulent Shear Flows," *Annual Review of Fluid Mechanics*, Vol. 16, 1984, pp. 263–285.

[9]Tam, C. K. W., "Supersonic Jet Noise," *Annual Review of Fluid Mechanics*, Vol. 27, 1995, pp. 17–43.

[10]Mani, R., Stringas, E. J., Wang, J. C. F., Balsa, T. F., Gliebe, P. R., and Kantola, R. A., "High Velocity Jet Noise Source Location and Reduction," Task 2, Federal Aviation Administration, Rept. FAA-RD-76-79-II, Cincinnati, OH, 1977.

[11]Ffowcs Williams, J. E., "The Noise from Turbulence Convected at High Speed," *Philosophical Transactions of the Royal Society of London, Series A: Mathematical and Physical Sciences*, Vol. A255, 1963, pp. 469–503.

[12]Khavaran, A., Krejsa, E. A., and Kim, C. M., "Computation of Supersonic Jet Mixing Noise from an Axisymmetric CD Nozzle Using (k–ε) Turbulence Model," AIAA Paper 92-0500, Jan. 1992.

[13]Baily, C., Bechara, W., Lafon, P., and Candel, S., "Jet Noise Predictions Using a (k–ε) Turbulence Model," AIAA Paper 93-4412, Oct. 1993.

[14]Baily, C., Lafon, P., and Candel, S., "Prediction of Supersonic Jet Noise from a Statistical Acoustic Model and a Compressible Turbulence Closure," *Journal of Sound and Vibration*, Vol. 194, No. 2, 1996, pp. 219–242.

[15]Tam, C. K. W., and Auriault, L., "Jet Mixing Noise from Fine-Scale Turbulence," *AIAA Journal*, Vol. 37, No. 2, 1999, pp. 145–153.

[16]Reynolds, O., "An Experimental Investigation of the Circumstances Which Determine Whether the Motion of Water will be Direct or Sinuous and the Law of Resistance in Parallel Channels," *Philosophical Transactions of the Royal Society of London*, Vol. 174, May 1883, pp. 935–950.

[17]Goldstein, M. E., *Aeroacoustics*, NASA SP-346, 1974, pp. 103–159.

[18]Batchelor, G. K., *The Theory of Homogeneous Turbulence*, Cambridge Univ. Press, Cambridge, England, U.K., 1953.

[19]Balsa, T. F., "The Acoustic Field of Sources in Shear Flow with Application to Jet Noise: Convective Amplification," *Journal of Fluid Mechanics*, Vol. 79, No. 1, 1977, pp. 33–40.

[20]Goldstein, M. E., "High Frequency Sound Emission from Moving Point Multipole Sources Embedded in Arbitrary Transversely Sheared Mean Flows," *Journal of Sound and Vibration*, Vol. 80, No. 4, 1982, pp. 499–512.

[21]Chen, Y. S., "FDNS—A General Purpose CFD Code, Version 4.0," Engineering Sciences, Inc., ESI-TR-97-01, Huntsville, AL, May 1997.

[22]Wang, T.-S., "Analysis of Linear Aerospike Plume-Induced X-33 Base-Heating Environment," *Journal of Spacecraft and Rockets*, Vol. 36, No. 6, 1999, pp. 777–783.

[23]Chen, Y.-S., and Kim, S. W., "Computation of Turbulent Flows Using an Extended k–ε Turbulence Closure Model," NASA CR-179204, Oct. 1987.

P. J. Morris
Associate Editor